Microstructural and mechanical behavior of second-phase hardened porous refractory Ti-Nb-Zr-Ta alloys

C. González-Guillén[a], L. Romero-Resendiz[b, c, d, *], M. Naeem[d], A. L. Vidilli[e], L. B. Otani[f], E. Klyatskina[a], G. Gonzalez[g, *], V. Amigó[a, *]

[a] Instituto de Tecnología de Materiales, Universitat Politècnica de València, Camino de Vera s/n, 46022 Valencia, Spain

[b] Facultad de Química, Departamento de Ingeniería Metalúrgica, Universidad Nacional Autónoma de México, Mexico City, 04510, Mexico

[c] Department of Design and Engineering, Faculty of Science and Technology, Bournemouth University, Poole, Dorset, BH12 5BB, UK

[d] School of Metallurgy and Materials, University of Birmingham, Birmingham, B15 2TT, UK

[e] Graduate Program in Materials Science and Engineering, Federal University of São Carlos, Rod. Washington Luiz, Km 235, São Carlos -SP, 13564-905, Brazil

[f] Department of Materials Engineering (DEMa), Federal University of São Carlos, Rod. Washington Luis, km 235, São Carlos –SP, 13565-905, Brazil.

[g] Instituto de Investigaciones en Materiales, Universidad Nacional Autónoma de México, Circuito exterior S/N, Cd. Universitaria, A. P. 70-360, Coyoacán, C.P. 04510, Mexico

*Corresponding authors: liliana.rom7@comunidad.unam.mx (L. R.-R.); joseggr@unam.mx (G. G.); vamigo@mcm.upv.es (V. A.)

Abstract

Second-phase hardening in refractory high-entropy alloys (RHEAs) has been recognized as one of the main routes to significantly improve their mechanical properties. However, their cost–benefit should not be compromised. Thus, we designed second-phase strengthened RHEAs by a low-cost powder metallurgy method. We induced the formation of FCC (face-centered cubic) ZrC second phase, which has not been reported in Ti-Nb-Zr-Ta alloys before and may be easily confused with the FCC-Zr due to the complexity of identifying carbon by conventional methods. We used neutron diffraction and electron backscatter diffraction for microstructural studies, as well as hardness, ultrasonic and compression techniques for assessing mechanical properties. Our investigation centered on equiatomic and equimassic Ti-Nb-Zr-Ta alloys, both displaying similar grain morphology and porosity but differing in grain sizes and phases. The variation in grain size was attributed to the influence of Ta as a grain growth pinning element. Our second-phase ZrC hardened alloys revealed higher stiffness and hardness, surpassing those documented in the existing literature.

Keywords

Refractory alloy; High-entropy alloy; Intermetallic; Microstructure; Mechanical properties

1. Introduction

Refractory high-entropy alloys (RHEAs) were reported in 2010 with the objective to overcome the technological challenge of building high-temperature-resistant components for aerospace, nuclear and chemical reactors [1]. RHEAs answer the immediate need for high mechanical properties at elevated temperatures, due to their high melting points, surpassing the commonly used nickel-based superalloys [2]. Microstructural control and the introduction of second-phase hardening in RHEAs have been recognized as the main routes to improve their mechanical properties [2]. Besides, increasing the multidisciplinary applications of RHEA is highly sought after area. So far, the effect of B2 and Laves phases as second-phase hardening of RHEAs has been broadly studied, but their formation requires thermo-mechanical processing that decreases the cost–benefit of the alloy. Seeking feasible and low-cost materials may be the biggest challenge for the technological application of materials science, including the second-phase hardened RHEAs.

In this work, we seek to explore the formation of carbides as a second-phase hardening route during the processing of the alloy, i.e., without further thermo-mechanical treatment. We selected a powder metallurgy method for promoting carbide formation during sintering. Powder metallurgy routes have been proven successful for obtaining carbide-reinforced RHEAs [3]. Besides, powder metallurgy is well recognized due to the minimized cost of machining complex-shaped components, as well as lower temperature and energetic requirement during processing compared to casting [4]. However, no multidisciplinary RHEA has explored this option yet. The Ti-Nb-Zr-Ta (TNZT) alloy was selected as the starting material because of its high oxidation and wear resistance [2], as well as low cytotoxic effect [5] of the constituent elements. Besides, Zr has a

high affinity to form carbides. Thus, the TNZT alloy is a RHEA with adequate physical, mechanical and biological properties for assessing the effect of second-phase hardening carbides.

Considering that carbon is difficult to characterize by conventional techniques, especially at low fraction content, we used neutron diffraction to demonstrate its presence and quantification in our alloys. The existence of an FCC Zr phase has been predicted from the elastic stability criteria [6]. Later, some works have reported its formation in pure elements [7,8] and alloys [9,10]. However, its phase transformation from the room-temperature-stable HCP-phase [10,11] is still not well understood. It has been usually linked to strain-induced or thermally-induced phase transformation [7,9,10]. The challenge in identifying carbon through conventional methods, coupled with ease with which carbon gets introduced from the environment during processing, may have previously obscured its role and impact in phase transformations.

In this work, we developed two second-phase hardened porous RHEAs based on TNZT alloy with the addition of a C-rich organic $C_{18}H_{36}O_2$ compound. Equiatomic and equimassic TNZT matrix were selected because they are the most commonly reported TNZT stoichiometries. Moreover, they offer broad literature to compare the new alloys produced in this work. We used neutron diffraction characterization to demonstrate the formation of FCC-ZrC phase.

2. Experimental methods

Before processing of the alloys, the phases predictions were carried out by thermodynamic calculations (CALPHAD method) using ThermoCalc® software and the TCHEA5 database. Once the formation of desired carbides was successfully simulated, commercial powders (Atlantic Equipment Engineers and Alfa Aesar) of Ti, Nb, ZrH_2, and Ta were used as raw materials for

producing the TNZT alloys (Table 1). The powders were weighed to obtain two second-phase hardened TNZT alloys as shown in Table 2.

Table 1. Raw powder characteristics.

Raw material	Purity / wt.%	Average particle size / μm	Crystal structure
Ti	99.9	44	HCP
Nb	99.8	1 - 5	BCC
ZrH_2	99.9	4.5 - 6.5	FCC
Ta	99.9	1 - 5	BCC

Table 2. Elemental composition of studied alloys.

	Equimassic TNZT		Equiatomic TNZT	
Element	**Wt. %**	**At. %**	**Wt. %**	**At. %**
Ti	24.75	43.22	11.34	24.65
Nb	24.75	22.27	22.25	24.91
Zr	24.75	22.68	21.84	24.91
Ta	24.75	11.43	43.57	25.05
$C_{18}H_{36}O_2$	1.00	0.39	1.00	0.49

Mechanical alloying (MA) was carried out in a planetary ball mill (Retsch model PM 400/2) at 350 rpm for 40 h. The milling was divided in work stages of 8 minutes on and 10 minutes off to improve the homogenization of alloys after press and sintering. Standard stainless-steel jars and chromium-steel balls with a ball-to-powder weight ratio of 10:1 were used for milling. 1 wt.% of

stearic acid ($C_{18}H_{36}O_2$) was used as a carbon source and debinding agent to avoid powder agglomeration. The powders were then compacted using a hydraulic press (Metallkraft model WPP 50 M) and a floating die of 1.8 cm^3 at 1,000 MPa for 10 seconds. The specimens were sintered in a high-vacuum tubular furnace (Carbolite HVT 15/75/450) at a pressure between 0.01 to 0.1 Pa in Ar atmosphere. Sintering was performed in three steps: 1) temperature increment at 5 °C min^{-1} until 800°C and holding for one hour, 2) temperature increment up to 1400°C and holding for three hours, and 3) furnace-cooling at 10 °C min^{-1} to room temperature.

Phase identification and estimation were carried out by neutron diffraction measurements at the TAKUMI beamline of the Materials and Life Science Experimental Facility (MLF) at the Japan Proton Accelerator Research Complex (J-PARC) with a collimator of 5 mm × 5 mm. For microstructural and mechanical properties characterisation, samples were prepared by conventional metallography and polishing with a colloidal solution of 0.3 μm silica. Morphological observations were done by electron backscatter diffraction (EBSD) in a Zeiss Auriga model scanning electron microscope with an HKLNordlys EBSD detector (15 KV). Energy dispersive X-ray spectroscopy (EDS) point and mapping analyses were performed in a scanning electron microscope (SEM) Zeiss ULTRA 55. Phase discrimination was performed by EBSD phase mappings through the "TruPhase" post-processing algorithm of Aztec software, which matches regions with similar chemical composition based on referenced EDS spectra previously obtained in the same sample. The content of C was inspected by a LECO ON836 Elemental Oxygen and Nitrogen Detection Analyzer. Porosity was estimated by the Archimedes method according to ASTM B962-17. At least five measurements were averaged for each sample.

The elastic modulus (E) was measured by ultrasonic non-destructive technique (Echograph 1090 from Karl Deutsch equipment) considering a Poisson's ratio of 0.34. At least 3 elastic

modulus measurements were obtained for statistical purposes. A Shimadzu Vickers HMV-2 microhardness tester was used for microhardness measurements ($HVN_{0.3}$) by applying 3 N for 15 s. At least 5 measurements were obtained per sample. A Shimadzu Autograph AG-100 KN Xplus universal testing machine was used for uniaxial compression testing at a strain rate of 0.5 mm min^{-1}. The tests were stopped before the barreling generated due to friction between the discs and the sample, which causes triaxial stress states and experimental errors in the stress-strain curves [12]. Yield strength was approximated by the 0.2% offset method. At least 3 compression tests were performed for statistical purposes.

3. Results and discussion

Based on the ThermoCalc® calculations presented in Fig. 1, it is anticipated that equimassic and equiatomic alloys will exhibit three phases, including the desired FCC-ZrC. The initial composition of 1.0 wt.% $C_{18}H_{36}O_2$ yields 0.76 wt.% of carbon. This specific carbon content was taken into account for generating Fig. 1a.1 and Fig.1b.1, as well as the phase compositions detailed in Table 3. Both alloys are expected to form BCC2 and FCC in the region 1500 to 600 °C. BCC2 phase have nearly equiatomic Ti, Nb and Ta contents, and a lower Zr concentration. FCC phase is enriched in C and Zr with depletion of Ti, Nb, and Ta. From 600 to 200 °C, BCC2, FCC, and BCC1 phases are formed in both alloys. BCC2 phase is mainly enriched in Nb and Ta with somewhat depletion of Ti and a low content of Zr between 3 to 4 at.%. The Nb, Ti, and Ta diffused out of the FCC phase, leaving a ZrC with 60 at.% of Zr and 40 at.% of C. The BCC1 phase is rich in Ti and Zr with lower contents of Nb and Ta. Below 200 °C, the FCC remains stable, while Zr and Ti have diffused from the BCC2 phase to form a new HCP phase, which has 62 to 75 at.% of

Ti and 25 to 38 at.% of Zr. Both equiatomic and equimassic alloys showed similar phase formation tendencies.

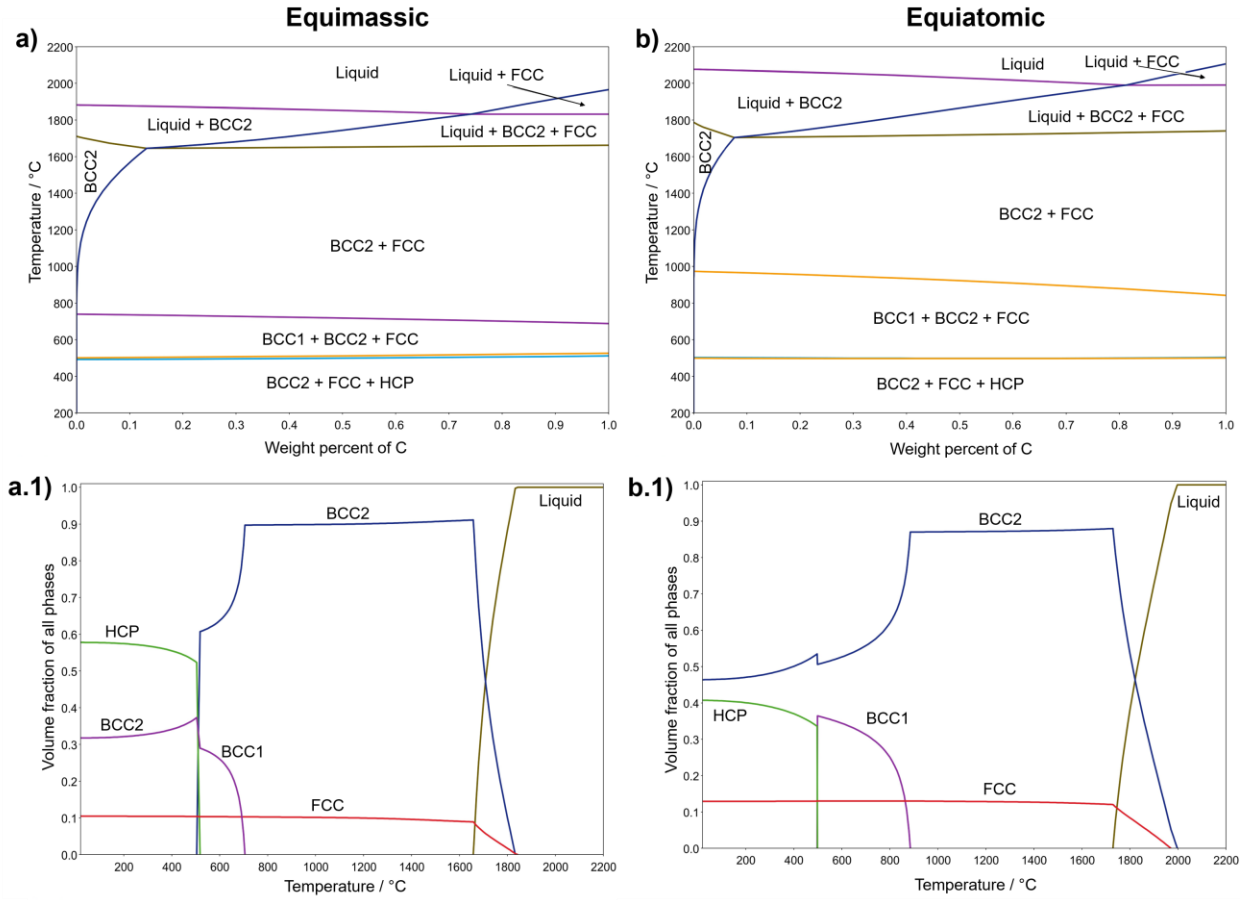

Fig. 1. a,b) Phase diagram and a.1., b.1.) cooling path of the a, a.1) equimassic and b, b.1) equiatomic TNZT alloys calculated by CALPHAD method.

146 **Table 3.** Chemical composition at the isopleth of 0.76% C from the phase diagram of equiatomic
147 and equimassic TNZT alloys.

Alloy	Temperature / °C	Phase	Composition
Equimassic TNZT	1500	BCC2	$Ti_{46}Nb_{23}Zr_{18}Ta_{12}C_{1}$
		FCC	$Ti_{10}Nb_{4}Zr_{44}Ta_{3}C_{39}$
	1000	BCC2	$Ti_{47}Nb_{24}Zr_{17}Ta_{12}$
		FCC	$Ti_{1}Nb_{1}Zr_{57}Ta_{1}C_{40}$
	600	BCC1	$Ti_{57}Nb_{15}Zr_{21}Ta_{7}$
		BCC2	$Ti_{23}Nb_{46}Zr_{4}Ta_{27}$
		FCC	$Zr_{60}C_{40}$
	200	HCP	$Ti_{75}Zr_{25}$
		BCC2	$Ti_{1}Nb_{65}Ta_{34}$
		FCC	$Zr_{60}C_{40}$
Equiatomic TNZT	1500	BCC2	$Ti_{27}Nb_{27}Zr_{18}Ta_{27}$
		FCC	$Ti_{4}Nb_{3}Zr_{50}Ta_{4}C_{39}$
	1000	BCC2	$Ti_{28}Nb_{27}Zr_{17}Ta_{28}$
		FCC	$Ti_{1}Nb_{1}Zr_{58}Ta_{1}C_{39}$
	600	BCC2	$Ti_{16}Nb_{39}Zr_{3}Ta_{42}$
		BCC1	$Ti_{48}Nb_{9}Zr_{38}Ta_{5}$
		FCC	$Zr_{60}C_{40}$
	200	BCC2	$Ti_{2}Nb_{49}Ta_{49}$
		HCP	$Ti_{62}Zr_{38}$
		FCC	$Zr_{60}C_{40}$

148

From neutron diffraction results, shown in Fig. 2 and Table 4, the equimassic TNZT sample (Fig. 2a) consisted of three phases, including two BCC ($Im\bar{3}m$) phases of lattice parameter 3.3060 Å (BCC1) and 3.3359 Å (BCC2), and one FCC ($Fm\bar{3}m$) phase with lattice parameter of 4.6016 Å. The larger lattice parameter of BCC2 compared to BCC1 agrees with its higher Ta content (Table 3), which is the constituent element with the largest atomic size. The equiatomic TNZT sample consisted of BCC1, FCC and HCP phases (Fig. 2b) with lattice parameters of 3.3148, 4.6092, and a=2.8960 and c=4.8999 Å, respectively. Some peaks remained unidentified in both patterns due to the probable oxidation during sintering and formation of complex oxides or carbides [13,14]. The unidentified peaks are very low in intensity and due to the structural complexity of the potential phases, they are expected in low amounts.

The predicted phases below 200 °C in Fig. 1 are different from the experimentally observed phases in Fig. 2. The difference between predicted and experimentally observed phases may come from the theoretical assumptions. The calculations in Fig. 1 did not consider that the starting powders do not melt during the press and sintering method. Thus, the TNZT alloys processed here by powder metallurgy route might have followed a different atomic diffusion path than the theoretical calculations. The predictions made by the CALPHAD method only show the thermodynamically stable phases and their quantities. The rate of solid-state diffusion (during sintering) is lower than in liquid state (assumption during the calculations). Therefore, the limited atomic diffusion could restrict the formation of the stable phases. The experimental results from Fig. 2 showed that the limited solid-state diffusion generated an equivalent effect to extending the BCC2 + BCC1 + FCC phase region to the room temperature in the equimassic TNZT alloy, and limiting HCP (only 4%) formation in the equiatomic alloy.

From the neutron diffraction data in Fig. 2, the FCC phase in the equimassic alloy (32.2%) is higher compared to the equiatomic alloy (25.3%) (Table 4). From Fig. 1 and Fig. 2, the FCC-ZrC phase is stable either at high-activated diffusion processes, like by assuming melting in the CALPHAD calculations, or during lower atomic diffusion processes like sintering at 1400 °C.

Figure 2c shows the simulated neutron diffraction profiles for Zr and ZrC with different Zr:C ratios. Increasing the carbon contents in the intermetallic ZrC causes the disappearance of three peaks located at 1.06, 1.39, and 2.66 Å. Despite the peak located at 2.66 Å is the most intense in the simulated patterns for 1:0.25 Zr:C ratio, neither the equimassic nor the equiatomic samples showed the presence of any of those three peaks. This evidence suggests that the ZrC has a high C percentage, while its similar lattice parameter in the equimassic (4.6016 Å) and equiatomic (4.6092 Å) alloys suggest a similar stoichiometry. Considering the significantly higher atomic mass of Zr (91.2 amu) compared to that of C (12.0 amu), a higher number of C atoms is expected for equivalent weights of Zr and C. Thus, a near-1:1 Zr:C atomic ratio may be possible for Zr-enriched regions. This stoichiometry agrees well with the refined carbon occupancy ratio of 0.475Zr:0.525C in the equiatomic alloy and 0.43Zr:0.57C in the equimassic alloy. Similar stoichiometry has been reported for FCC-ZrC with C distributed among octahedral interstitial sites [15]. Evidence of local Zr enrichments will allow observing the FCC-ZrC distribution and morphology.

Energy-dispersive X-ray spectroscopy (EDS) elemental mapping for equimassic and equiatomic TNZT alloys are shown in Fig. 3. A part of Zr is distributed in the matrix forming solid solution with Ti, Nb and Ta, i.e., forming the BCC phases. However, Zr-enriched zones were evident by the higher Zr presence at Ti, Nb and Ta-depleted zones. Thus, Zr-enriched zones may correspond to FCC-ZrC intermetallic and HCP-phase predicted by thermocalc simulations in Fig. 1 and confirmed by neutron diffraction in Fig. 2. Thus, the light regions in Fig. 3 correspond to

BCC phases while the dark regions correspond to FCC and HCP phases. The identification of these regions agrees well with point EDS analyses shown in Table 5 which showed Zr-enriched dark regions, which correspond to the HCP and FCC compositions (Table 3). Besides, homogeneously dispersed BCC1, BCC2, and FCC phases in the TNZT alloys were confirmed by EBSD shown in Fig. 4.

The presence of C was shown by an organic-elements analyzer, resulting in 0.814 and 0.851 wt.% for the equiatomic and equimassic TNZT alloys, respectively. These values are close to the nominal content of C of 0.76 wt% according to the nominal stearic acid content of 1.0 wt.% in each sample.

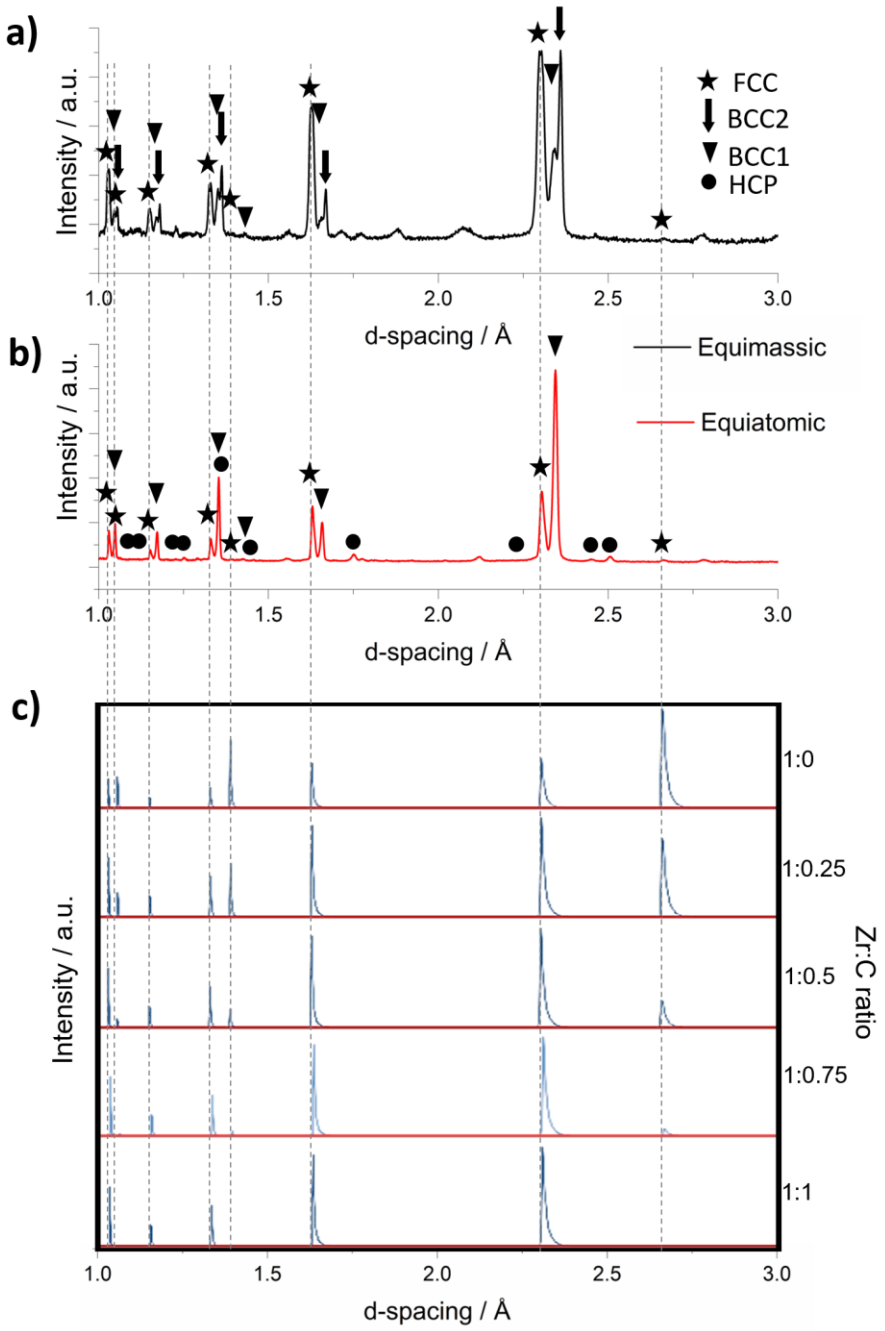

203

204 **Fig. 2.** Neutron diffraction patterns of a) equimassic and b) equiatomic TNZT alloys and their

205 comparison with c) simulated patterns of different Zr:C atomic ratios.

206

Table 4. Experimental lattice parameter of equimassic and equiatomic TNZT alloys calculated from neutron diffraction measurements.

Phase	Equimassic TNZT		Equiatomic TNZT	
	Lattice parameter Å	Phase percentage vol. %	Lattice parameter Å	Phase percentage vol. %
BCC1	a = 3.3060	30.4	a = 3.3148	70.7
BCC2	a = 3.3359	37.4	-	-
HCP	-	-	a = 2.8960 c = 4.8999	4.0
FCC	a = 4.6016	32.2	a = 4.6092	25.3

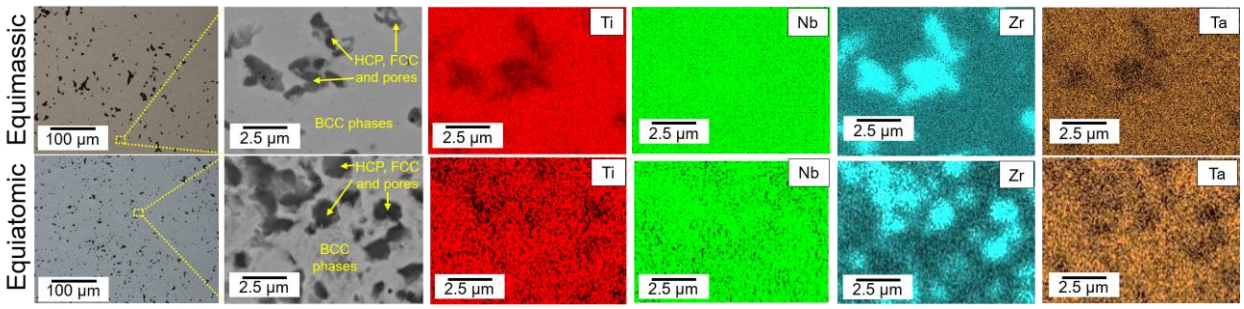

Fig. 3. EDS mapping of equimassic (upper panel) and equiatomic (lower panel) TNZT alloys.

Table 5. EDS point analyses of equimassic and equiatomic TNZT samples.

Element	Dark zones		Light zones	
	Wt.%	At.%	Wt.%	At.%
Ti	7.0 ± 0.1	13.2 ± 0.3	12.7 ± 0.3	28.2 ± 0.6
Nb	5.7 ± 0.1	5.6 ± 0.1	24.8 ± 0.5	28.4 ± 0.6
Zr	76.4 ± 1.5	75.8 ± 1.5	11.3 ± 0.2	13.2 ± 0.3
Ta	10.9 ± 0.2	5.5 ± 0.1	51.2 ± 1.0	30.2 ± 0.6

From Fig. 4c,d, both alloys showed nearly equiaxed grain morphology. The grain size of the equimassic is bigger than the equiatomic TNZT alloy. The quantitative differences in grain size are shown in Table 6, where there are two types of averages, the standard and the area-weighted. The first one represents the average when the maximum grain size is dominated by the diameter of the grains that exist in higher number. On the other hand, in the second type the maximum grain size is dominated by the diameter of the largest grains. The larger grain size of the equimmasic alloy agrees with the lower quantity of Ta compared to those in the equiatomic alloy (Table 2). As the Ta atomic weight (180.9 amu) is the highest among the constituent elements (Ti = 47.8; Nb = 92.9; Zr = 91.2; C = 12.0 amu), a lower quantity of Ta atoms corresponds to the same weight percent in the equimassic TNZT alloy. The lower Ta diffusion compared to the other constituent elements in TNZT alloys has been reported [16]. Due to the large difference of Ta atomic weight, many physical phenomena, including higher density and lower diffusion are expected. Low element diffusion is commonly correlated with grain growth anchor due to pinning effect. This has been observed in powder metallurgy processed $Ti_{25+x}Nb_{25}Zr_{25}Ta_{25-x}$ (X = 0, 5, and 10) alloys, where the higher the Ta, the lower the grain size [16]. To evaluate the effect of the microstructural features on the mechanical properties, hardness, compression and ultrasonic techniques were applied.

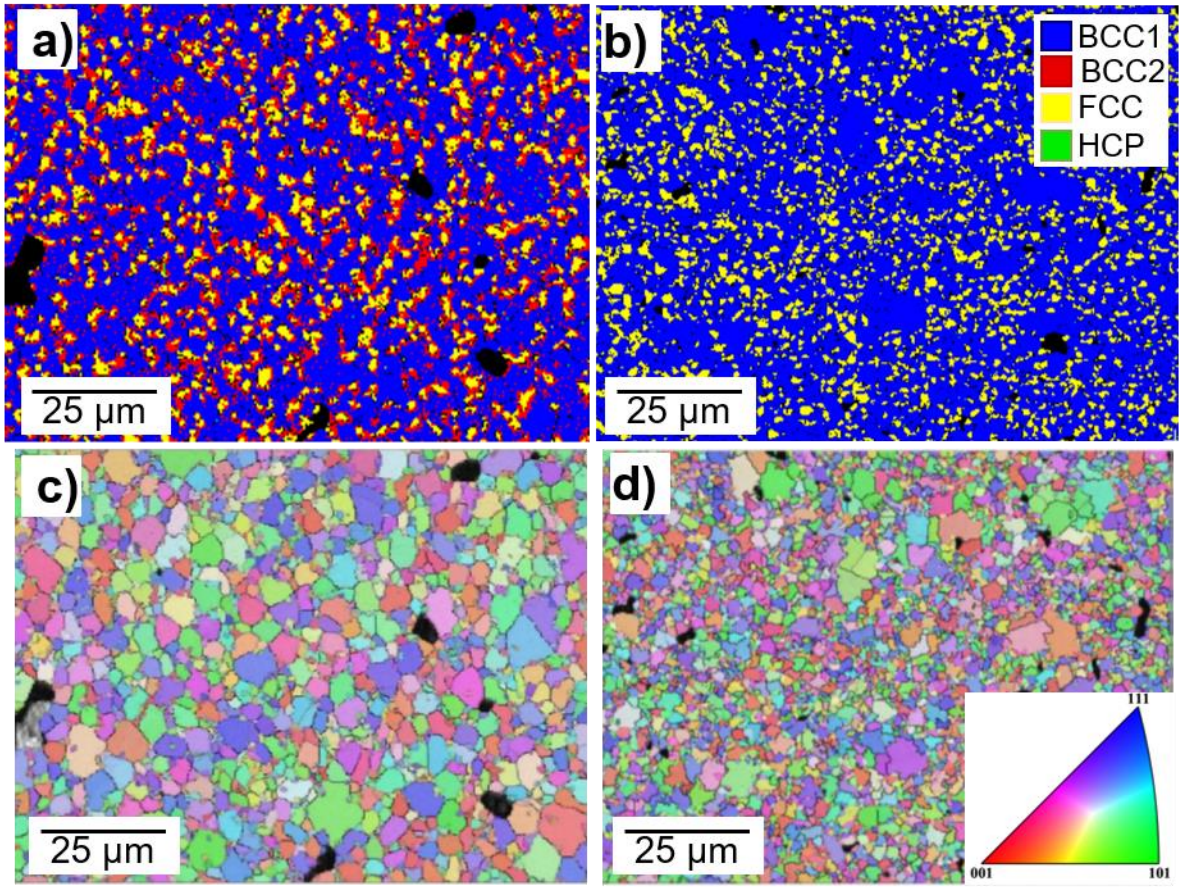

Fig. 4. EBSD a,b) phase contrast mappings and c,d) inverse pole figure mapping of the a,c) equimassic and b,d) equiatomic TNZT alloys.

Table. 6. Grain size of the equimassic and equiatomic TNZT alloys.

Alloy	Min / μm	Max / μm	Standard mean / μm	Area-weighted mean / μm	Standard deviation / μm
Equimassic	1.4	10.6	3.0	4.6	1.5
Equiatomic	1.1	7.9	1.9	3.0	0.9

Table 7 shows the results of mechanical properties, where it can be observed that the equimassic alloy has 6.9% higher hardness than the equiatomic alloy. Meanwhile, the stiffness indicated by

241 the elastic modulus is 16.4% higher for the equiatomic. A directly proportional trend between
242 hardness and stiffness can be expected in dense materials. However, porous materials, such as the
243 studied TNZT alloys, might follow a different trend as a function of the applied load during
244 mechanical testing. In a similar way, porous zirconia toughened alumina has been reported with
245 variable hardness values depending on the indentation load [17]. This phenomenon is related to
246 densification and pore collapse during loading. As shown in Fig. 4, both equimassic and
247 equiatomic alloys possess the typical porous microstructure by powder metallurgy processing
248 route (Table 8). Thus, the different tendency between hardness and elastic modulus might be
249 related to the applied load during hardness measurements, while the ultrasonic testing does not
250 involve the application of mechanical loads. This hypothesis is also in agreement with the higher
251 precision for determination of elastic properties reported by dynamic methods compared to
252 mechanical tests [18]. It is noteworthy that the hardness values of the equiatomic and equiatomic
253 alloys might overlap considering the measurement deviation indicated in Table 7. The comparable
254 hardness of both alloys could be due to their similar total porosity (Table 8), equiaxed grain
255 morphology (Fig. 4), and elemental distribution (Fig. 3).

256

257 **Table 7.** Mechanical properties of ZrC-containing TNZT alloys evaluated by microhardness,
258 ultrasonic and compression testing.

TNZT alloy	$HVN_{0.3}$	E / GPa	Ultimate strength / MPa	Yield strength / MPa
Equimassic	489.1 ± 35.0	111.2 ± 0.0	1178.9 ± 149.7	865 ± 109.8
Equiatomic	455.2 ± 20.7	133.0 ± 0.0	1229.2 ± 158.2	1005 ± 129.3

259

260

Table 8. Porosity of the studied TNZT alloys.

TNZT alloy	Open porosity / %	Closed porosity / %	Total porosity / %
Equimassic	2.71 ± 1.07	2.53 ± 0.39	5.86 ± 0.70
Equiatomic	0.95 ± 0.90	4.17 ± 0.11	5.12 ± 0.97

On the other hand, the strongest contribution to elastic modulus of metallic materials comes from the atomic bonding instead of from microstructural features, such as grain size [19]. Then, the higher elastic modulus (Table 7) in the equiatomic alloy may be related to local interatomic bonding disparities due to the presence of HCP phase in addition to the FCC phase that is present in both alloys (Table 4). As the BCC matrix contents of both alloys is similar (67.8 and 70.7% for equimassic and equiatomic alloys), its effect has been discussed with the reported TNZT alloys in literature. As shown in Fig. 6, reported TNZT alloys with at least 90% of BCC phase produced by melting or powder metallurgy have elastic moduli ranging from 73 to 91 GPa [16,20]. Contrastingly, the TNZT alloys with 67.8 to 70.7% of BCC phase produced in this work, showed higher elastic moduli ranging from 11.2 to 133 GPa. Thus, the highest contribution to the elastic modulus of the TNZT alloys came from the phase contents, where the BCC phase seems to decrease the elastic modulus of TNZT alloys. Besides, phase contents, the TNZT alloys also showed different grain sizes. However, its effect can be considered negligible when the grain is larger than some dozens of nanometers [19,21]. To distinguish better the effect of the microstructural differences between both alloys, i.e., phase contents and grain size, compression testing was performed.

Figure 5 shows the stress vs. strain curves obtained from compression testing in the equimassic and equiatomic TNZT alloys. The mechanical properties obtained from compression testing are included in Table 7. The 4.1 and 13.9% higher ultimate and yield strength for the equiatomic alloy

compared to the equimassic one are within the experimental errors. Thus, as hardness, the ultimate and yield strengths of both TNZT alloys are comparable. From hardness and compression testing, which are techniques with a strong dependence on microstructural features, it is suggested that the microstructural differences between both samples (given by grain size and phases contents) did not have a significant contribution to cause a substantial change of mechanical properties.

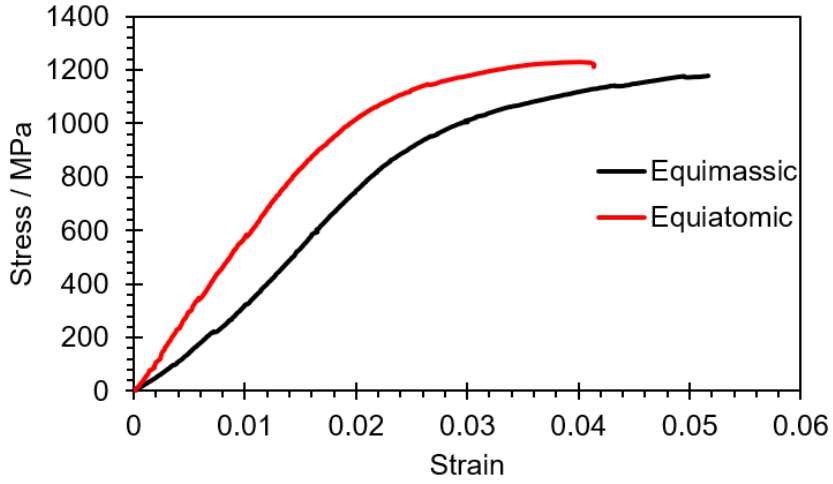

Fig. 5. Stress vs strain curves obtained from compression testing in the equimassic and equiatomic TNZT alloys.

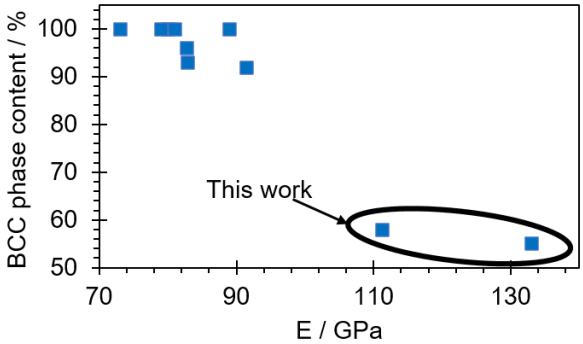

Fig. 6. Elastic modulus as a function of the BCC phase contents on reported TNZT alloys [16,20] and the ones produced in this work.

The strong effect of second-phase hardening particles can also be observed by comparing the hardness and stiffness of reported RHEA with the equimassic and equiatomic second-phase hardened TNZT alloys of this work (Fig. 7). Despite the alloys from the literature have similar chemical composition to the second-phase hardened TNZT alloys in this work, they have shown somewhat lower hardness and Young's modulus. Thus, the FCC-ZrC second-phase hardening was proven as a successful strategy for improving mechanical properties of refractory TNZT alloys. This hardening strategy in TNZT alloys was more efficient than the use of dispersed α-Ti particles reported elsewhere (Fig. 7a) [22].

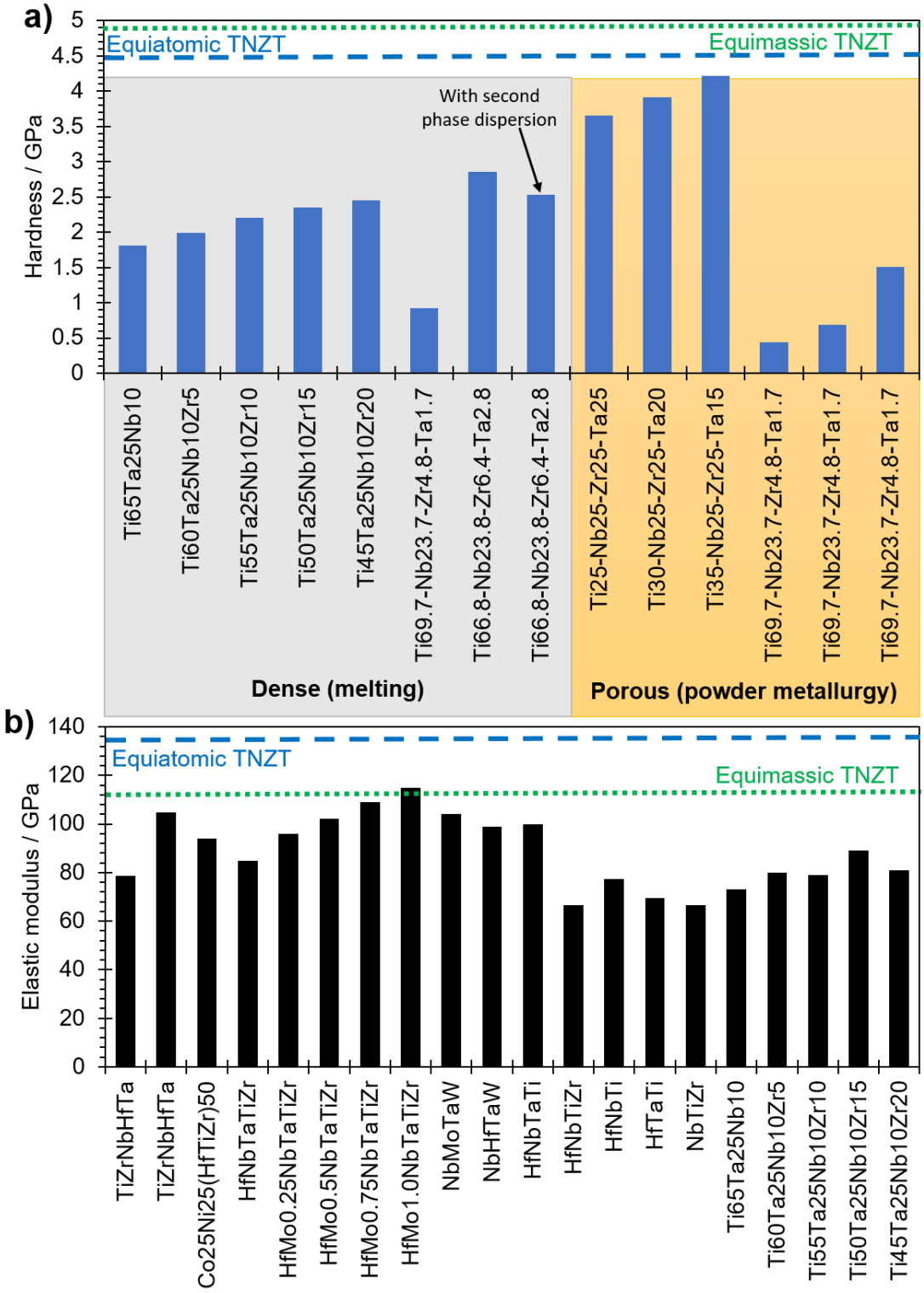

Fig. 7. Comparison of a) hardness [16,20,22–24] and b) elastic modulus [20,25–29] of the TNZT alloys of this study (blue and green dashed lines) with other RHEAs from the literature.

Conclusions

Equimassic and equiatomic second-phase hardened TiZrNbTa alloys were produced by powder metallurgy method. An organic $C_{18}H_{36}O_2$ compound was added before sintering for promoting the formation of FCC-ZrC intermetallic in the BCC matrix. Both alloys showed similar grain morphology and porosity but different grain size and phases. Equimassic alloy showed two BCC and one FCC phase with mean grain size of 4.6 μm, while the equiatomic alloy showed BCC, HCP, and FCC phases with mean grain size of 3.0 μm. The different grain size was related to the effect of Ta as grain growth pinning element. The equimassic alloy showed a higher FCC-phase content and larger area-weighted grain size (32.2 % and 4.6 μm) compared to the equiatomic alloy (20.20 % and 3.0 μm). While the hardness and strength of both alloys can be considered comparable considering porosity and statistical deviation effects, the stiffness slightly increased in the equiatomic alloy (133.0 GPa) compared to the equimassic alloy (111.2 GPa). The higher stiffness may be related to local interatomic bonding disparities promoted by the presence of HCP phase in addition to the FCC phase which is present in both alloys.

Acknowledgments

LRR acknowledges the funding from the Programa de Apoyo a la Investigación y el Posgrado (PAIP-50009223) of the Chemistry College of Universidad Nacional Autónoma de México, as well as from the Programa de Apoyo a Proyectos de Investigacion e Innovacion Tecnologica (PAPIIT)-UNAM under grant number IA102724. MN thanks the Asia-Oceania Neutron Scattering Association (AONSA) for the award of the AONSA Young Research Fellowship (AONSA-YRF-

2022). ALV acknowledges FAPESP for financial support in his internship at UPV under the grant number 2021/11537–1. GG acknowledges PAPIIT-UNAM under grant number IN110124. VA acknowledges the funding from the Spanish Ministerio de Ciencia, Innovación y Universidades with project RTI2018-097810-B-I00, and the European Commission via European Regional Development Fund (FEDER). The neutron diffraction experiments were performed at TAKUMI in MLF of J-PARC.

Data Availability

The raw data related to this manuscript would be made available on request.

Conflict of interest

The authors declare that there are no conflicts of interest.

CRediT author statement

C. González-Guillén: Conceptualization, Methodology, Investigation. **L. Romero-Resendiz:** Supervision, Visualization, Writing-Original Draft. **M. Naeem:** Investigation (neutron diffraction), Formal analysis, Writing - Review & Editing. **A. Vidilli:** Methodology (diagram phase simulation), Writing - Review & Editing. **L. B. Otani:** Resources (Thermocalc), Writing - Review & Editing. **E. Klyatskina:** Conceptualization, Writing - Review & Editing. **G. Gonzalez:** Supervision, Visualization, Writing - Review & Editing. **V. Amigó:** Resources, Supervision, Visualization, Funding acquisition, Writing - Review & Editing.

References

[1] O.N. Senkov, G.B. Wilks, D.B. Miracle, C.P. Chuang, P.K. Liaw, Refractory high-entropy alloys, Intermetallics. 18 (2010) 1758–1765. https://doi.org/10.1016/j.intermet.2010.05.014.

[2] W. Xiong, A.X.Y. Guo, S. Zhan, C.T. Liu, S.C. Cao, Refractory high-entropy alloys: A focused review of preparation methods and properties, J. Mater. Sci. Technol. 142 (2023) 196–215. https://doi.org/10.1016/j.jmst.2022.08.046.

[3] S. Lv, Y. Zu, G. Chen, X. Fu, W. Zhou, An ultra-high strength CrMoNbWTi-C high entropy alloy co-strengthened by dispersed refractory IM and UHTC phases, J. Alloys Compd. 788 (2019) 1256–1264. https://doi.org/10.1016/j.jallcom.2019.02.318.

[4] W.B. James, Powder Metallurgy Methods and Applications, Powder Metall. 7 (2018) 9–19. https://doi.org/10.31399/asm.hb.v07.a0006022.

[5] S.S. Sidhu, H. Singh, M.A.H. Gepreel, A review on alloy design, biological response, and strengthening of β-titanium alloys as biomaterials, Mater. Sci. Eng. C. 121 (2021) 111661. https://doi.org/10.1016/j.msec.2020.111661.

[6] A. Aguayo, G. Murrieta, R. de Coss, Elastic stability and electronic structure of fcc Ti, Zr, and Hf: A first-principles study, Phys. Rev. B - Condens. Matter Mater. Phys. 65 (2002) 921061–921064. https://doi.org/10.1103/PhysRevB.65.092106.

[7] X. Hu, H. Zhao, S. Ni, M. Song, Grain refinement and phase transition of commercial pure zirconium processed by cold rolling, Mater. Charact. 129 (2017) 149–155. https://doi.org/10.1016/j.matchar.2017.04.037.

[8] W. Guo, F. Han, G. Li, Y. Zhang, M. Ali, J. Ren, Q. Wang, F. Yuan, Atomic scale investigation of FCC → HCP reverse phase transformation in face-centered cubic zirconium, J. Mater. Sci. Technol. 137 (2022) 8–13. https://doi.org/10.1016/j.jmst.2022.07.032.

[9] C. Liu, G. Li, H. Gu, F. Yuan, F. Han, M. Ali, Y. Zhang, W. Guo, Observation of FCC-Zr phase in as-cast Zircaloy-4 alloy, Mater. Lett. 267 (2020) 127551. https://doi.org/10.1016/j.matlet.2020.127551.

[10] B. Tao, R. Qiu, Y. Liu, X. Tan, Q. Liu, FCC phase transformation of Zr alloy during air cooling and aging, J. Nucl. Mater. 551 (2021) 152989. https://doi.org/10.1016/j.jnucmat.2021.152989.

[11] M.T. Pérez-Prado, A.A. Gimazov, O.A. Ruano, M.E. Kassner, A.P. Zhilyaev, Bulk nanocrystalline ω-Zr by high-pressure torsion, Scr. Mater. 58 (2008) 219–222. https://doi.org/10.1016/j.scriptamat.2007.09.043.

[12] X. Wang, H. Li, K. Chandrashekhara, S.A. Rummel, S. Lekakh, D.C. Van Aken, R.J. O'Malley, Inverse finite element modeling of the barreling effect on experimental stress-strain curve for high temperature steel compression test, J. Mater. Process. Technol. 243 (2017) 465–473. https://doi.org/10.1016/j.jmatprotec.2017.01.012.

[13] L.N. Miotto, L.M.G. Fais, A.L.R. Ribeiro, L.G. Vaz, Surface properties of Ti-35Nb-7Zr-5Ta: Effects of long-term immersion in artificial saliva and fluoride solution, J. Prosthet. Dent. 116 (2016) 102–111. https://doi.org/10.1016/j.prosdent.2015.10.024.

[14] S.J. Li, R. Yang, S. Li, Y.L. Hao, Y.Y. Cui, M. Niinomi, Z.X. Guo, Wear characteristics of Ti-Nb-Ta-Zr and Ti-6Al-4V alloys for biomedical applications, Wear. 257 (2004) 869–876. https://doi.org/10.1016/j.wear.2004.04.001.

[15] T. Davey, K. Suzuki, H. Miura, Y. Chen, Stability and structural properties of vacancy-ordered and -disordered ZrCx, RSC Adv. 11 (2021) 32573–32589. https://doi.org/10.1039/d1ra06362f.

[16] G. Al Hawajreh, G. Gonzalez, L. Romero-Resendiz, A. Vidilli, L.B. Otani, V. Amigó, Effect of the Ti/Ta ratio on the feasibility of porous Ti25+x-Nb25-Zr25-Ta25-x (X= 0, 5, and 10) alloys for biomedical applications, J. Mater. Res. Technol. (2023) 109181. https://doi.org/10.1016/j.jmrt.2023.04.070.

[17] A. Nastic, A. Merati, M. Bielawski, M. Bolduc, O. Fakolujo, M. Nganbe, Instrumented and Vickers Indentation for the Characterization of Stiffness, Hardness and Toughness of Zirconia Toughened Al2O3 and SiC Armor, J. Mater. Sci. Technol. 31 (2015) 773–783. https://doi.org/10.1016/j.jmst.2015.06.005.

[18] M. Radovic, E. Lara-Curzio, L. Riester, Comparison of different experimental techniques for determination of elastic properties of solids, Mater. Sci. Eng. A. 368 (2004) 56–70. https://doi.org/10.1016/j.msea.2003.09.080.

[19] H.S. Kim, M.B. Bush, Effects of grain size and porosity on the elastic modulus of nanocrystalline materials, Nanostructured Mater. 11 (1999) 361–367. https://doi.org/10.1016/S0965-9773(99)00052-5.

[20] G. Ji, Z. Zhou, F. Meng, X. Yang, R. Sheng, J. Qiao, P.K. Liaw, M. Li, L. Jiang, S. Chen, Y. Tong, Effect of Zr addition on the local structure and mechanical properties of Ti–Ta–Nb–Zr refractory high-entropy alloys, J. Mater. Res. Technol. 19 (2022) 4428–4438. https://doi.org/10.1016/j.jmrt.2022.06.160.

[21] P. Sharma, S. Ganti, On the grain-size-dependent elastic modulus of nanocrystalline materials with and without grain-boundary sliding, J. Mater. Res. 18 (2003) 1823–1826. https://doi.org/10.1557/JMR.2003.0253.

[22] S. Nag, R. Banerjee, H.L. Fraser, Microstructural evolution and strengthening mechanisms in Ti-Nb-Zr-Ta, Ti-Mo-Zr-Fe and Ti-15Mo biocompatible alloys, Mater. Sci. Eng. C. 25 (2005) 357–362. https://doi.org/10.1016/j.msec.2004.12.013.

[23] M.C. Rossi, B.N. Ventura, L. Milián, A.V. Escuder, V.A. Borrás, Study of Electrochemical and Biological Characteristics of As-Cast Ti-Nb-Zr-Ta System Based on Its Microstructure, Metals (Basel). 12 (2022). https://doi.org/10.3390/met12030476.

[24] J. Rechtin, E. Torresani, E. Ivanov, E. Olevsky, Fabrication of Titanium-Niobium-Zirconium-Tantalium Alloy (TNZT) bioimplant components with controllable porosity by spark plasma sintering, Materials (Basel). 11 (2018). https://doi.org/10.3390/ma11020181.

[25] M. Moschetti, A. Xu, B. Schuh, A. Hohenwarter, J.P. Couzinié, J.J. Kruzic, D.

Bhattacharyya, B. Gludovatz, On the Room-Temperature Mechanical Properties of an Ion-Irradiated TiZrNbHfTa Refractory High Entropy Alloy, Jom. 72 (2020) 130–138. https://doi.org/10.1007/s11837-019-03861-6.

[26] Q. He, S. Yoshida, N. Tsuji, Characteristic strengthening mechanisms in body-centered cubic refractory high/medium entropy alloys, Scr. Mater. 231 (2023) 115442. https://doi.org/10.1016/j.scriptamat.2023.115442.

[27] C.C. Juan, K.K. Tseng, W.L. Hsu, M.H. Tsai, C.W. Tsai, C.M. Lin, S.K. Chen, S.J. Lin, J.W. Yeh, Solution strengthening of ductile refractory HfMoxNbTaTiZr high-entropy alloys, Mater. Lett. 175 (2016) 284–287. https://doi.org/10.1016/j.matlet.2016.03.133.

[28] Q.F. He, J.G. Wang, H.A. Chen, Z.Y. Ding, Z.Q. Zhou, L.H. Xiong, J.H. Luan, J.M. Pelletier, J.C. Qiao, Q. Wang, L.L. Fan, Y. Ren, Q.S. Zeng, C.T. Liu, C.W. Pao, D.J. Srolovitz, Y. Yang, A highly distorted ultraelastic chemically complex Elinvar alloy, Nature. 602 (2022) 251–257. https://doi.org/10.1038/s41586-021-04309-1.

[29] J. Mo, Y. Wan, Z. Zhang, B. Shen, X.B. Liang, The structure and mechanical properties of NbHfTaW refractory high-entropy alloy: A combined theoretical and experimental study, Int. J. Refract. Met. Hard Mater. 111 (2023) 106067. https://doi.org/10.1016/j.ijrmhm.2022.106067.